atoms

MDPI

Article

Probing the Fragmentation Pathways of an Argon Dimer in Slow Ion–Dimer Collisions

Md Abul Kalam Azad Siddiki, Lokesh C. Tribedi and Deepankar Misra *

Department of Nuclear and Atomic Physics, Tata Institute of Fundamental Research, Mumbai 400005, India
* Correspondence: dmisra@tifr.res.in

Abstract: We report the development of a supersonic jet assembly to study electron transfer collisions with atoms, molecules, and van der Waals clusters. A comparative study of Ar monomer and dimer cations is presented for different capture-associated channels with a 2.5 keV/u O^{2+} projectile beam. For the Ar^{+} + Ar^{+} fragmentation channel, the interatomic relaxation channels are discussed. The vacancies of the dimer single site or double site show the dependence on capture mechanisms. In the Ar^{2+} + Ar^{+} fragmentation channel, double capture, in addition to the single ionization process, dominates. The orientation effect reflects the maximum yield at around 50 and 130 degrees, and angular distributions are nearly symmetric about the axis perpendicular to the dimer axis.

Keywords: electron capture; interatomic relaxation processes; dimer fragmentation; orientation effect

check for updates

Citation: Siddiki, M.A.K.A.; Tribedi, L.C.; Misra, D. Probing the Fragmentation Pathways of an Argon Dimer in Slow Ion–Dimer Collisions. *Atoms* **2023**, *11*, 34. https://doi.org/10.3390/atoms11020034

Academic Editors: Izumi Murakami, Daiji Kato, Hiroyuki A. Sakaue and Hajime Tanuma

Received: 28 December 2022
Revised: 20 January 2023
Accepted: 8 February 2023
Published: 9 February 2023

1. Introduction

The study of multiple-electron transfer collisions with atoms/molecules has raised many fundamental questions due to the involvement of various capture mechanisms. However, capture cross-section and angular distributions are essential to understand the charge exchange dynamics in various applied areas [1,2]. To test the effect on the environment, van der Waals dimers, where two centers are separated by a few Angstroms (Å), are the perfect candidates. In these weakly bound systems, a new kind of energy transfer mechanism known as interatomic Coulombic decay (ICD) was first theoretically reported by Cederbaum et al. [3]. With the development of multiparticle momentum imaging techniques such as cold-target recoil-ion momentum spectroscopy (COLTRIMS) [4,5], the signature of ICD has been reported experimentally [6,7]. ICD electrons have very low energy, typically less than 10 eV. These secondary electrons can be attached to molecules via the dissociative electron attachment (DEA) process [8] and result in bond breaking [9]. Many experiments have been reported to explore this new relaxation channel using synchrotron radiation [10], free electron lasers (FELs) [11], ion accelerators [12–14], etc. Recently, collision studies on molecular and cross-dimers enhanced the understanding of the environmental effect on fragmentation dynamics [15,16].

For the ion–dimer collision study on the impact of a charged particle, the Argon dimer (Ar_2) serves as a clean prototype system. Matsumoto et al. [17] studied the relaxation channel arising from the single-site double-valence electron holes. When two electrons from a single site of the Ar dimer are captured, it results in the $Ar^{2+}(3p^{-2}) - Ar(3p^{0})$ state. This state decays to Ar^{+} $(3p^{-1}\})$ + Ar^{+} $(3p^{-1}\})$ via transferring an electron to Ar^{2+}, in addition to a photon. This relaxation is known as radiative charge transfer (RCT), a slow process in the nanosecond (*ns*) regime [18]. Ren et al. [19] controlled the RCT and ICD relaxation processes by varying the projectile electron energies around their respective threshold. The electron capture radius and the projectile final states in slow collisions depend on the incoming projectile charge states. Low-charged projectiles with multiple ($\geq$ 2)-electron capture radii smaller than the dimer internuclear separations can lead to more efficient site-selective capture. After the collision, electronically excited dimer cations

can decay to repulsive states through various relaxation processes with timescales ranging from nanoseconds (*ns*) to femtoseconds (*fs*) [18]. Therefore, the interplay between electronic and vibrational motions also emerges. The corresponding potential energy is converted to the kinetic energy of the fragment ions, known as kinetic energy release (KER). As these repulsive states are Coulombic, one can easily calculate the corresponding internuclear separation. KER distributions (KERDs) act as a probe for the relaxation mechanism that arises due to the involvement of a single site or double site. The cross-section of the various capture-associated mechanisms is strongly governed by the impact parameter of collisions. The literature [20,21] shows that in the slow ion–atom collision regime, single capture (SC) has the maximum cross-section, followed by single ionization (SI) and transfer ionization (TI = SC + SI), and the smallest one characterizes double ionization (DI). Therefore, studying fragmentation pathways for each capture-associated mechanism could result in a different yield. Under low-energy conditions, collisions of highly charged ions (HCIs) and Ar_2 result in preferential near-site electron capture [17]. It would be interesting to see the orientation effect on low-charged projectile ions in slow collisions.

In this article, we studied electron capture collision using a 2.5 keV/u $O^{2+-}Ar_2$ collision system. The relative yield of monomer and dimer cations was analyzed for different capture mechanisms. We investigated the Ar^+ + Ar^+ and Ar^{2+} + Ar^+ fragmentation pathways in detail. The orientation effect of Ar^{2+} + Ar fragmentation on the dominant capture channel was also discussed.

2. Experimental Methods

The experiments were performed in the electron cyclotron resonance-based ion accelerator (ECRIA) [22] facility at TIFR, Mumbai, using the home-built COLTRIMS setup [23]. The 2.5 keV/u O^{2+} projectile beam interacted perpendicularly with the supersonic Ar jet. Before the interaction chamber, a cylindrical electrostatic beam cleaner was used to avoid the primary projectile beam contamination due to beamline electron capture with residual gases. After the electron capture process, the charge-changing projectiles were analyzed using an electrostatic charge state analyzer (CSA). The main projectile beam was deflected towards a Faraday cup, and the other charge-changing ions were detected by with a projectile detector (MCP + DLD). The recoil ions were guided by the vertical electric fields and detected with a recoil detector (MCP + DLD). Both recoil and projectile MCPs were 80 mm in diameter. The data were stored in event-by-event list mode using Cobold PC software for offline analysis. The electric fields in the extraction and acceleration regions were 86.67 V/cm and 125.33 V/cm, respectively, which ensured 6.5 eV 4π collection for singly charged recoil ions. To compensate for the projectile beam deflection due to the spectrometer fields, we used electrostatic deflector pairs. A pair of four jaw slits were also used in the beamline to reduce the beam current to the optimal operational value. Details can be found elsewhere [23]. The beam current at the final Faraday cup was maintained at around ~125 pA. Figure 1 presents the schematic picture of the complete experimental setup.

Supersonic jet assembly: The supersonic jet was produced by means of the expansion of Ar gas at a stagnation pressure of 2.5 bar towards the discharge vacuum chamber (~10^{-8} mbar) through a 30 μm nozzle. During this isentropic process, the whole energy is converted into the directed motion, and the gas cools down [24]. This results in small relative velocities among gas particles. If this relative kinetic energy is smaller than the binding energy of the dimer and the excess energy due to dimerization is carried away as a form of kinetic energy by a third particle, the dimer is produced through three-body collisions. Behind the nozzle, the zone of silence region was extracted by the first skimmer of 400 μm in diameter. Another skimmer of 750 μm in diameter further collimated it to cut down the large transverse momentum component. This resulted in geometrical cooling, which further cooled down the temperature from a few K to mK perpendicular to the jet propagation direction. The separation between the two skimmers was 40 mm. The nozzle-to-interaction-region distance was around ~130 mm. The target was finally dumped into the dump chamber, separated from the main interaction chamber by a 200 mm conductance-

limiting tube. With this geometry, the width of the target in the interaction region was estimated at around ~2.1 mm. The velocity of the Ar supersonic jet was calculated to be about ~550 m/s. All chambers were differentially pumped. The pumping speeds of the turbo-molecular pumps for discharge, skimmer, interaction, and dump chambers were 700, 300, 700, and 300 L/s, respectively. In Table 1, we show the gauge readings [24] before and after gas expansion. The pressure rise in the dump chamber was more than an order of magnitude greater than that in the interaction chamber. Therefore, we used the following formula to calculate the target density [25]:

$$\rho = \frac{N_A}{22.4} \frac{\Delta p_{dump}\, L_{dump}}{v_{jet} \frac{\pi}{4} d_t^2}, \tag{1}$$

where N_A is Avogadro's constant, and Δp_{dump} (bar) and L_{dump} (l/s) are the pressure enhancement and the pumping speed in the dump chamber. Using Table 1 parameters and the multiplication factor for the gauge reading and the pumping speed, we found the target density to be around ~10^{11} cm^{-3} for Ar gas.

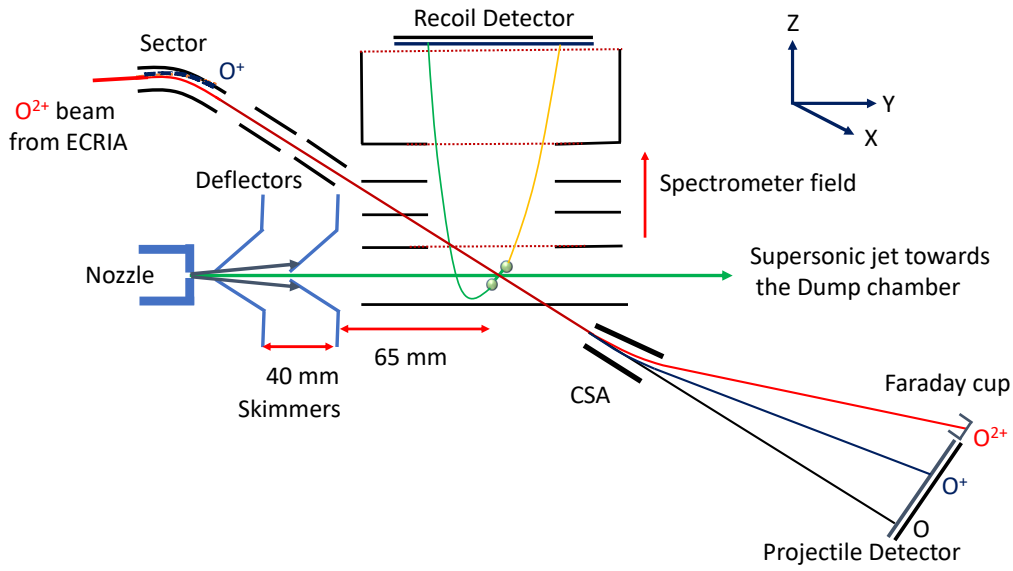

Figure 1. Schematic picture of the electron capture system, including the supersonic jet assembly. Dimensions are not to scale.

Table 1. Gauge readings of the differential chambers before and after the 2.5 bar Ar jet expansion.

Differential Chamber	Before Jet (mbar)	After Jet (mbar)
Discharge	2.2×10^{-8}	1.1×10^{-4}
Skimmer	1.4×10^{-8}	1.7×10^{-6}
Interaction	7.4×10^{-9}	8.6×10^{-9}
Dump	1.4×10^{-8}	4.5×10^{-8}

3. Results and Discussions

The time-of-flight (TOF) spectra in Figure 2 show the singly, doubly, and triply charged monomer concentrations. The higher fraction of Ar^{2+} compared with Ar^{+} indicates the near-resonant double-electron capture in the O^{2+}-Ar collision system. The binding energy differences were minimized for capturing both electrons in the O($2s^2\ 2p^4$) or O($2s^2\ 2p^3\ 3l$) state. We also compared the relative yields of Ar^{2+} and Ar^{3+} cations for each capture channel. In Table 2, we show the measured yields. The right-most small peak around 12000 ns shows the signature of singly charged Ar_2^{+} dimer cations resulting from the SC events. This reflects the production of neutral Ar_2 during supersonic jet expansion. The

fraction of dimer to monomer was in the order of 10^{-3}. In Figure 3 (left), we show the ion–ion coincidence plot. The various Ar_2 dimer fragmentation channels are indicated for different capture channels. Here, Ar^+ + Ar^+ and Ar^{2+} + Ar^+ are visible. For different capture-associated processes, the relative yields for all fragmentation channels are tabulated in Table 3. As in the monomer case, the DC channel was also the dominant one for the dimer. The distributions of the different capture channels are plotted for each fragmentation in Figure 3 (right). For the DC + SI process, the population of the Ar^{2+} + Ar^+ channel was enhanced remarkably compared with the monomer tri-cations. We cannot see any trace of Ar^{3+} + Ar^+ and Ar^{2+} + Ar^{2+} fragmentation channels in the coincidence plot. In this experiment, we did not detect the O^- projectile ion resulting from triple-electron capture. The binding energy of O^- is about ~1.46 eV [26], which can easily autoionize and mix with the DC channel. However, the inelasticity of this endothermic reaction is large, which reduces the probability of such events. The cross-sections for triple-electron capture and single ionization (TC + SI) are also expected to be small due to smaller capture radii. Contributions from the other, less probable double capture in addition to double ionization (DC + DI) or the single capture in addition to the triple ionization (SC + TI) process were not observed.

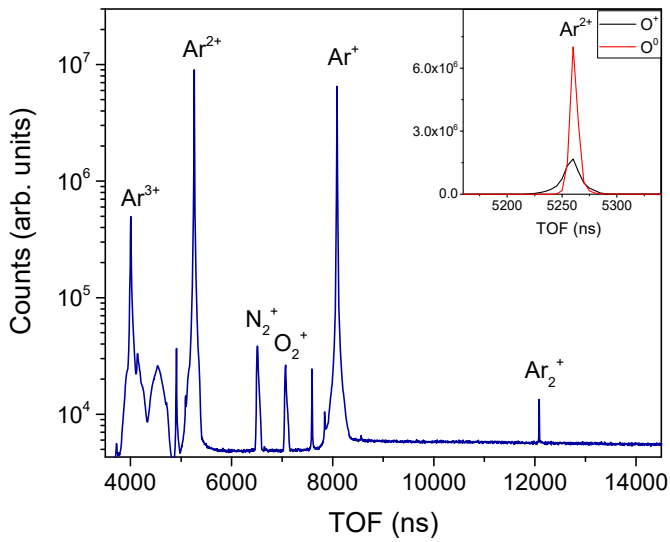

Figure 2. The TOF spectrum contains the monomer and dimer cations. In the inset, the yield of Ar^{2+} monomer di-cation is shown for TI and DC channels.

Table 2. Relative yields of Ar^{2+} and Ar^{3+} with respect to the sum of Ar^{2+} and Ar^{3+} contributions for the involved capture channels.

Ion	Capture Channel	Relative Yield
Ar^{2+}	DC	0.6162
Ar^{2+}	TI	0.3202
Ar^{3+}	DC + SI	0.0495
Ar^{3+}	SC + DI	0.014

Table 3. Relative yields for the resulted fragmentation channels for associated capture mechanisms.

Fragmentation Channel	Capture Channel	Relative Yield
Ar^+ + Ar^+	DC	0.5261
Ar^+ + Ar^+	TI/TE	0.2814
Ar^{2+} + Ar^+	DC + SI /SC + TI	0.1760
Ar^{2+} + Ar^+	SC + DI /SI + TI	0.0164

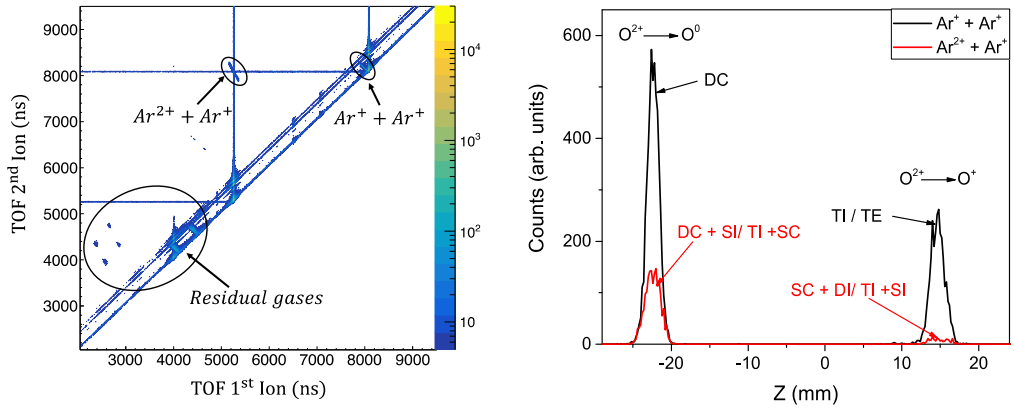

Figure 3. Ion–ion coincidence spectrum for O^{2+}-Ar_2 collision system (**left**). The projection of the charge-changing projectile ions for the various capture channels in coincidence with Ar^+ + Ar^+ and Ar^{2+} + Ar^+ fragmentation pathways (**right**).

3.1. Fragmentation of $Ar_2{}^{2+}$

In the electron capture processes in the O^{2+}-Ar_2 collision system, the Ar^+ + Ar^+ fragmentation channel may arise from a pure double capture (DC), transfer ionization (TI), or transfer excitation (TE) process. For low-charged projectiles such as O^{2+}, the principal quantum numbers of the captured electrons in the final projectile states are around (2, 2) or (2, 3). These states do not belong to the autoionization regions where the projectile can autoionize after double-electron capture. Therefore, the fragmentation in coincidence with O^+ projectiles mainly arises from the TI or, in some cases, the TE process.

The different relaxation channels were as follows:

$$O^{2+} + Ar_2 \rightarrow O^0 + Ar^{2+}\left(3p^{-2}\right) - Ar \rightarrow O^0 + Ar^+\left(3p^{-1}\right) + Ar^+\left(3p^{-1}\right) \text{ (single − site DC)} \quad (2)$$

$$O^{2+} + Ar_2 \rightarrow O^0 + Ar^+\left(3p^{-1}\right) + Ar^+\left(3p^{-1}\right) \text{ (double − site DC)} \quad (3)$$

$$O^{2+} + Ar_2 \rightarrow O^+ + Ar^{2+}\left(3p^{-2}\right) - Ar + e^- \rightarrow O^+ + Ar^+\left(3p^{-1}\right) + Ar^+\left(3p^{-1}\right) \text{ (single − site TI)} \quad (4)$$

$$O^{2+} + Ar_2 \rightarrow O^+ + Ar^+\left(3p^{-1}\right) + Ar^+\left(3p^{-1}\right) + e^- \text{ (double − site TI)} \quad (5)$$

$$O^{2+} + Ar_2 \rightarrow O^+ + Ar^{+*}\left(3p^{-2}nl\right) - Ar+ \rightarrow O^+ + Ar^+\left(3p^{-1}\right) + Ar^+\left(3p^{-1}\right) + e_{ICD} \text{ (single − site TE)} \quad (6)$$

As the electron mobility between the two centers was small, we could consider them separate atoms. In this regard, the cross-section for DC was almost twice that of the TI process in the monomer cases. Figure 4 (left) shows the KERDs for both capture channels. Both RCT and ICD processes are schematically shown in Figure 4 (right). As the RCT process is slow, it achieves vibrational motion, and the radiative decay mostly occurs in the inner turning point. Hence, the large KER peak around ~5.2 eV arose from the RCT process. With the approximation of the pure Coulomb repulsive state, we obtained $R\left(\text{Å}\right) = \frac{14.4 q_1 q_2}{KER\ (eV)}$, where q_1 and q_2 are the charged centers. The corresponding internuclear distance from the KERDs obtained was around ~2.77 Å. Matsumoto et al. [17] calculated the KER tail of the RCT to be 3.5 eV, which is the result of the weighted contribution from the other excited vibration states and the R-dependent radiative decay probability. The low KER peak was around ~3.65 eV, resulting from the two-site DC process, which arose from the direct Coulomb explosion (CE) from $Ar^+\left(3p^{-1}\right) + Ar^+\left(3p^{-1}\right)$ at near-equilibrium distance ($R_{eq} \sim 3.8$Å). The heights of the KER peaks originating from these two processes widely differed. In the DC process, the dominance of the RCT process was due to the quasi-resonant single-site DC process. The double-site capture radius of around 2.74 Å

was calculated using the classical over-the-barrier (COB) model [27,28]. The capture radius smaller than R_{eq} also resulted in a smaller KER yield at 3.65 eV. It has been reported [17,29] that in collisions of highly charged ions and Ar_2 where the capture radii are well over R_{eq}, double-site capture is dominant, resulting in a higher yield of low KER peaks. In the TI process, the KER peak heights in the two processes (direct CE and RCT) were almost equal. We cannot ignore the TE process, where the projectile captures one *3p* electron, and another *3p* electron is excited to higher states, such as $Ar^{+*}\left(3p^{-2}nl\right) - Ar\left(3p^{0}\right)$, where *nl* could be *3d*, *4s*, *5s*, or *5d* [18,19]. This subsequently decays to $Ar^{+}\left(3p^{-1}\right) + Ar^{+}\left(3p^{-1}\right)$ states via slow and fast ICD decay processes.

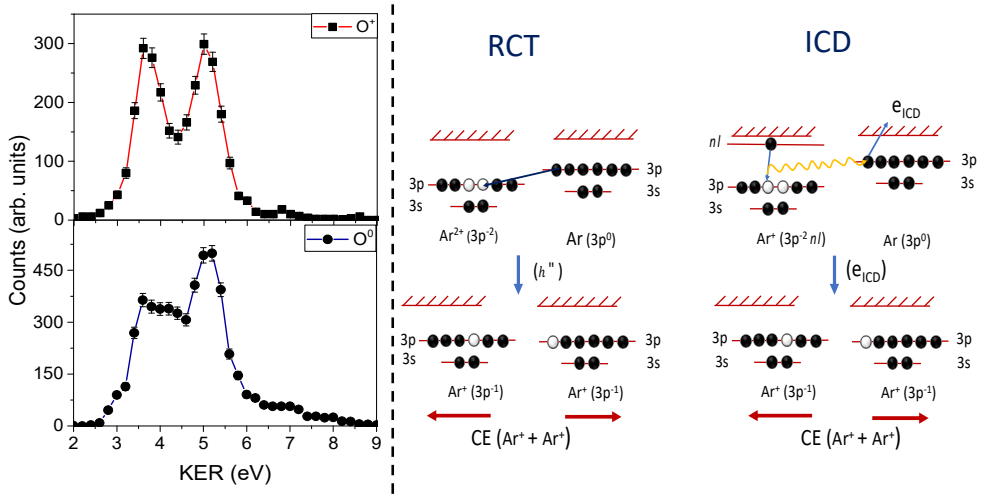

Figure 4. KERDs for Ar^{+} +Ar^{+} channel for associated capture channels (**left**). Two interatomic relaxation channels are shown schematically (**right**).

Small contributions in the high KER region (6 to 9 eV) mostly arise from single-site $(3s^{-1}3p^{-1})$ captures. After that, a charge transfer (CT) process occurs at the intersection of the two pathways of capture and fragmentation as follows [29]:

$$O^{2+} + Ar_2 \rightarrow O^0 + Ar^{2+}\left(3s^{-1}3p^{-1}\right) - Ar \rightarrow O^0 + Ar^{+*}\left(3p^{-2}nl\right) + Ar^{+}\left(3p^{-1}\right) \quad (7)$$

3.2. Fragmentation of Ar_2^{3+}

For Ar^{2+} + Ar^{+} fragmentation, the four possible capture-associated channels were as follows:

$$O^{2+} + Ar_2 \rightarrow O^0 + Ar^{2+}\left(3p^{-2}\right) + Ar^{+}\left(3p^{-1}\right) + e^{-} \quad (\mathrm{DC + SI\ /\ TI + SC}) \quad (8)$$

and

$$O^{2+} + Ar_2 \rightarrow O^{+} + Ar^{2+}\left(3p^{-2}\right) + Ar^{+}\left(3p^{-1}\right) + 2e^{-} \quad (\mathrm{SI + TI\ /\ SC + DI}) \quad (9)$$

Around ~92% of Ar^{2+} + Ar^{+} events occurred in coincidence with neutral O. The KERDs for the associated capture channels are shown in Figure 5 (left). The KER peak was around ~7.4 eV, reflecting the electron involvement in both centers, and resulted from the direct fragmentation of Ar^{2+} + Ar^{+}. The small peak was about ~10 eV, implying the initial Ar^{3+}-Ar channel, which further decayed to Ar^{2+} + Ar^{+} [30]. The two possible capture pathways were DC + SI and TI + SC. Here, the capture channels are defined by their site-selective contributions. In this O^{2+}-Ar_2 collision system, DC was the near-resonant process; therefore, the DC + SI channel could have had a higher yield than TI + SC. On the other hand, in coincidence with the O^{+} projectile ion, SI + TI and SC + DI were the possible channels that had a sufficiently low yield compared with the combination of DC + SI and TI + SC.

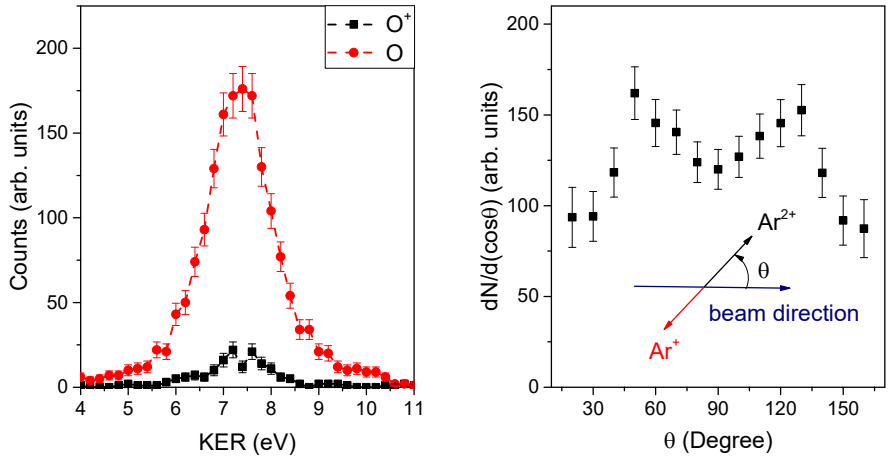

Figure 5. KERDs for Ar^{2+} + Ar^{+} channel for associated capture channels (**left**). The orientation effect for dominant DC + SI channels (**right**).

To see the orientation effect of the involved dominant capture channel, we plotted the angular distribution (refer to Figure 5 (right)) with respect to the projectile beam axis of the KER region of 6 to 8.5 eV. To obtain the dissociation time, we numerically solved the equation of motion of the charged dimer centers in a Coulomb potential using Wolfram Mathematica. It showed that 90% of the potential energy was converted to kinetic energy in around ~400 fs, and the corresponding internuclear separation was ~30 Å. This dissociation time is relatively fast compared with the rotational period (~200 picoseconds). Hence, the axial recoil approximation [31] is valid for the direct fragmentation channel.

Figure 5 (right) shows the maximum yields at ~50 and 130 degrees. After that, it slightly reduced to 90 degrees, and around 20 and 160 degrees, it resulted in the lowest yield. From 20 to 160 degrees, the angular distribution was nearly symmetric with respect to the axis perpendicular to the dimer axis. Therefore, it did not have a specific preference between near-site and far-site DC, i.e., both DC + SI and SI + DC seemed equally probable. Here, we define the near site as the first center that the projectile encounters, which is backward with respect to the projectile direction. We interpreted the cross-section variation using geometrical arguments, as it is directly related to the impact parameters or capture radius. DC had a yield comparable to that of SC, which resulted in a large impact parameter. The deflection of the projectile, due to the transverse momentum transfer, occurred away from the collision plane as the distance increased. Therefore, the near-parallel orientation where the distance between the centers was large ($R_{eq} \cos\theta$) resulted in a lower yield. On the other hand, between 50 and 130 degrees, it seems that after encountering the near site, deflection occurred towards the far site and resulted in a large yield by lowering the impact parameter. For dimer perpendicular orientation, the impact parameters were found to mainly lie on the midplane of the dimer axis to access both centers for the associated capture radii.

4. Conclusions

We report the performance of a new supersonic jet assembly to study electron transfer collisions with an Ar dimer. We present the comparative study of different relaxation processes for the Ar^{+} + Ar^{+} fragmentation channel. For the near-resonant DC process, the RCT process largely dominated over the direct CE process. For the direct Ar^{2+} + Ar^{+} fragmentation pathways, the DC +SI capture channel resulted in the most significant yield. The orientation effect is explained in terms of impact parameters.

Author Contributions: Conceptualization, M.A.K.A.S., L.C.T. and D.M.; formal analysis, M.A.K.A.S. and D.M.; investigation, M.A.K.A.S., L.C.T. and D.M.; data curation, M.A.K.A.S. and D.M.; writing—original draft preparation, M.A.K.A.S.; writing—review and editing, M.A.K.A.S., L.C.T. and D.M.; resources, M.A.K.A.S., L.C.T. and D.M.; funding acquisition, L.C.T. and D.M.; supervision, D.M. All authors have read and agreed to the published version of the manuscript.

Funding: This work was supported by the Department of Atomic Energy (Government of India), research project RTI 4002.

Data Availability Statement: The data are available upon reasonable request from the authors.

Acknowledgments: We thank Kamal Kumar and Jibak Mukherjee for their help during jet alignment and ECRIA operation. We would also like to thank TIFR Central Workshop for the machining of the jet assembly.

Conflicts of Interest: The authors declare no conflict of interest.

References

1. Kraft, G. Radiobiological effects of highly charged ions. In *The Physics of Multiply and Highly Charged Ions*; Springer: Berlin/Heidelberg, Germany, 2003; pp. 149–196.
2. Beiersdorfer, P.; Boyce, K.; Brown, G.; Chen, H.; Kahn, S.; Kelley, R.; May, M.; Olson, R.; Porter, F.; Stahle, C.; et al. Laboratory simulation of charge exchange-produced X-ray emission from comets. *Science* **2003**, *300*, 1558–1559. [CrossRef] [PubMed]
3. Cederbaum, L.; Zobeley, J.; Tarantelli, F. Giant intermolecular decay and fragmentation of clusters. *Phys. Rev. Lett.* **1997**, *79*, 4778. [CrossRef]
4. Dörner, R.; Mergel, V.; Jagutzki, O.; Spielberger, L.; Ullrich, J.; Moshammer, R.; Schmidt-Böcking, H. Cold target recoil ion momentum spectroscopy: A 'momentum microscope'to view atomic collision dynamics. *Phys. Rep.* **2000**, *330*, 95–192. [CrossRef]
5. Ullrich, J.; Moshammer, R.; Dorn, A.; Dörner, R.; Schmidt, L.P.H.; Schmidt-Böcking, H. Recoil-ion and electron momentum spectroscopy: Reaction-microscopes. *Rep. Prog. Phys.* **2003**, *66*, 1463. [CrossRef]
6. Marburger, S.; Kugeler, O.; Hergenhahn, U.; Möller, T. Experimental evidence for interatomic Coulombic decay in Ne clusters. *Phys. Rev. Lett.* **2003**, *90*, 203401. [CrossRef]
7. Jahnke, T.; Czasch, A.; Schöffler, M.; Schössler, S.; Knapp, A.; Käsz, M.; Titze, J.; Wimmer, C.; Kreidi, K.; Grisenti, R.; et al. Experimental observation of interatomic Coulombic decay in neon dimers. *Phys. Rev. Lett.* **2004**, *93*, 163401. [CrossRef]
8. Pan, X.; Cloutier, P.; Hunting, D.; Sanche, L. Dissociative electron attachment to DNA. *Phys. Rev. Lett.* **2003**, *90*, 208102. [CrossRef]
9. Boudaıffa, B.; Cloutier, P.; Hunting, D.; Huels, M.A.; Sanche, L. Resonant formation of DNA strand breaks by low-energy (3 to 20 eV) electrons. *Science* **2000**, *287*, 1658–1660. [CrossRef]
10. Jahnke, T. Interatomic and intermolecular Coulombic decay: The coming of age story. *J. Phys. B At. Mol. Opt. Phys.* **2015**, *48*, 082001. [CrossRef]
11. Schnorr, K.; Senftleben, A.; Kurka, M.; Rudenko, A.; Foucar, L.; Schmid, G.; Broska, A.; Pfeifer, T.; Meyer, K.; Anielski, D.; et al. Time-resolved measurement of interatomic Coulombic decay in Ne 2. *Phys. Rev. Lett.* **2013**, *111*, 093402. [CrossRef]
12. Titze, J.; Schöffler, M.; Kim, H.K.; Trinter, F.; Waitz, M.; Voigtsberger, J.; Neumann, N.; Ulrich, B.; Kreidi, K.; Wallauer, R.; et al. Ionization dynamics of helium dimers in fast collisions with He++. *Phys. Rev. Lett.* **2011**, *106*, 033201. [CrossRef]
13. Kim, H.K.; Titze, J.; Schöffler, M.; Trinter, F.; Waitz, M.; Voigtsberger, J.; Sann, H.; Meckel, M.; Stuck, C.; Lenz, U.; et al. Enhanced production of low energy electrons by alpha particle impact. *Proc. Natl. Acad. Sci. USA* **2011**, *108*, 11821–11824. [CrossRef]
14. Kim, H.K.; Gassert, H.; Titze, J.; Waitz, M.; Voigtsberger, J.; Trinter, F.; Becht, J.; Kalinin, A.; Neumann, N.; Zhou, C.; et al. Orientation dependence in multiple ionization of He 2 and Ne 2 induced by fast, highly charged ions: Probing the impact-parameter-dependent ionization probability in 11.37-MeV/u S 14+ collisions with He and Ne. *Phys. Rev. A* **2014**, *89*, 022704. [CrossRef]
15. Méry, A.; Agnihotri, A.; Douady, J.; Fléchard, X.; Gervais, B.; Guillous, S.; Iskandar, W.; Jacquet, E.; Matsumoto, J.; Rangama, J.; et al. Role of a neighbor ion in the fragmentation dynamics of covalent molecules. *Phys. Rev. Lett.* **2017**, *118*, 233402. [CrossRef]
16. Zhu, X.; Hu, X.; Yan, S.; Peng, Y.; Feng, W.; Guo, D.; Gao, Y.; Zhang, S.; Cassimi, A.; Xu, J.; et al. Heavy N+ ion transfer in doubly charged N2Ar van der Waals cluster. *Nat. Commun.* **2020**, *11*, 2987. [CrossRef]
17. Matsumoto, J.; Leredde, A.; Flechard, X.; Hayakawa, K.; Shiromaru, H.; Rangama, J.; Zhou, C.; Guillous, S.; Hennecart, D.; Muranaka, T.; et al. Asymmetry in multiple-electron capture revealed by radiative charge transfer in Ar dimers. *Phys. Rev. Lett.* **2010**, *105*, 263202. [CrossRef]
18. Miteva, T.; Chiang, Y.C.; Kolorenc, P.; Kuleff, A.; Gokhberg, K.; Cederbaum, L. Interatomic Coulombic decay following resonant core excitation of Ar in argon dimer. *J. Chem. Phys.* **2014**, *141*, 064307. [CrossRef]
19. Ren, X.; Jabbour Al Maalouf, E.; Dorn, A.; Denifl, S. Direct evidence of two interatomic relaxation mechanisms in argon dimers ionized by electron impact. *Nat. Commun.* **2016**, *7*, 11093. [CrossRef] [PubMed]
20. Groh, W.; Muller, A.; Schlachter, A.; Salzborn, E. Transfer ionisation in slow collisions of multiply-charged ions with atoms. *J. Phys. B At. Mol. Phys.* **1983**, *16*, 1997. [CrossRef]

21. Wu, W.; Cocke, C.; Giese, J.; Melchert, F.; Raphaelian, M.; Stöckli, M. Observation of direct ionization of He by highly charged ions at low velocity. *Phys. Rev. Lett.* **1995**, *75*, 1054. [CrossRef]
22. Agnihotri, A.; Kelkar, A.; Kasthurirangan, S.; Thulasiram, K.; Desai, C.; Fernandez, W.; Tribedi, L. An ECR ion source-based low-energy ion accelerator: Development and performance. *Phys. Scr.* **2011**, *2011*, 014038. [CrossRef]
23. Siddiki, M.A.K.A.; Nrishimhamurty, M.; Kumar, K.; Mukherjee, J.; Tribedi, L.C.; Khan, A.; Misra, D. Development of a cold target recoil ion momentum spectrometer and a projectile charge state analyzer setup to study electron transfer processes in highly charged ion–atom/molecule collisions. *Rev. Sci. Instrum.* **2022**, *93*, 113313. [CrossRef] [PubMed]
24. Miller, D.R.; Scoles, G. Atomic and molecular beam methods. *At. Mol. Beam Methods* **1988**, *1*, 14.
25. Jahnke, T. "Interatomic Coulombic Decay": Experimentelle Untersuchung eines neuartigen, interatomaren Abregungsmechanismus. Ph.D. Thesis, Goethe University Frankfurt am Main, Frankfurt, Germany, 2005.
26. Kristiansson, M.K.; Chartkunchand, K.; Eklund, G.; Hole, O.M.; Anderson, E.K.; de Ruette, N.; Kamin'ska, M.; Punnakayathil, N.; Navarro-Navarrete, J.E.; Sigurdsson, S.; et al. High-precision electron affinity of oxygen. *Nat. Commun.* **2022**, *13*, 5906. [CrossRef] [PubMed]
27. Niehaus, A. A classical model for multiple-electron capture in slow collisions of highly charged ions with atoms. *J. Phys. B At. Mol. Phys.* **1986**, *19*, 2925. [CrossRef]
28. Bárány, A.; Astner, G.; Cederquist, H.; Danared, H.; Huldt, S.; Hvelplund, P.; Johnson, A.; Knudsen, H.; Liljeby, L.; Rensfelt, K.G. Absolute cross sections for multi-electron processes in low energy Arq+- Ar collisions: Comparison with theory. *Nucl. Instrum. Methods Phys. Res. Sect. B Beam Interact. Mater. At.* **1985**, *9*, 397–399. [CrossRef]
29. Iskandar, W. Étude Des Collisions à Basse Énergie Entre Ions Multichargés et Dimères de Gaz Rare. Ph.D. Thesis, Université de Caen Normandie, Caen, France, 2015.
30. Zhu, X.; Yan, S.; Feng, W.; Ma, X.; Chuai, X.; Guo, D.; Gao, Y.; Zhang, R.; Zhang, P.; Zhang, S.; et al. Orientation effect in Ar dimer fragmentation by highly charged ion impact. *J. Phys. B At. Mol. Opt. Phys.* **2018**, *51*, 155204. [CrossRef]
31. Zare, R.N. Dissociation of H2+ by electron impact: Calculated angular distribution. *J. Chem. Phys.* **1967**, *47*, 204–215. [CrossRef]